Research Article

Preparation and toughening mechanism of Al$_2$O$_3$ composite ceramics toughened by B$_4$C@TiB$_2$ core–shell units

Yingjie Shi[a], Weixing Li[a], Xiaorong Zhang[a,b,*], Jiachao Jin[a], Jilin Wang[c], Yu Dong[d],
Jingbo Mu[a], Guangsuo Wang[a], Xiaoliang Zhang[a], Zhixiao Zhang[a,*]

[a]*Key Laboratory of New Inorganic Nonmetallic Composites of Handan, College of Materials
Science and Engineering, Hebei University of Engineering, Handan 056038, China*
[b]*Key Laboratory of Intelligent Industrial Equipment Technology of Hebei Province, College of Mechanical
and Equipment Engineering, Hebei University of Engineering, Handan 056038, China*
[c]*College of Materials Science and Engineering, Guilin University of Technology, Guilin 532100, China*
[d]*School of Civil and Mechanical Engineering, Curtin University, Perth 6845, Australia*

Abstract: In this paper, the concept of incorporating core–shell structured units as secondary phases to toughen Al$_2$O$_3$ ceramics is proposed. Al$_2$O$_3$ composite ceramics toughened by B$_4$C@TiB$_2$ core–shell units are successfully synthesized using a combination of molten salt methodology and spark plasma sintering. The synthesis of B$_4$C@TiB$_2$ core–shell toughening units stems from the prior production of core–shell structural B$_4$C@TiB$_2$ powders, and this core–shell structure is effectively preserved within the Al$_2$O$_3$ matrix after sintering. The B$_4$C@TiB$_2$ core–shell toughening unit consists of a micron-sized B$_4$C core enclosed by a shell approximately 500 nm in thickness, composed of numerous nanosized TiB$_2$ grains. The regions surrounding these core–shell units exhibit distinct geometric structures and encompass multidimensional variations in phase composition, grain dimensions, and thermal expansion coefficients. Consequently, intricate stress distributions emerge, fostering the propagation of cracks in multiple dimensions. This behavior consumes a considerable amount of crack propagation energy, thereby enhancing the fracture toughness of the Al$_2$O$_3$ matrix. The resulting Al$_2$O$_3$ composite ceramics display relative density of 99.7%±0.2%, Vickers hardness of 21.5±0.8 GPa, and fracture toughness 6.92±0.22 MPa·m$^{1/2}$.

Keywords: Al$_2$O$_3$ composite ceramics; microstructure design; core–shell structure; toughening mechanism; spark plasma sintering (SPS)

* Corresponding authors.

E-mail: X. Zhang, xrzhang611@163.com;

　　　Z. Zhang, zhixiao351@hebeu.edu.cn

1 Introduction

Alumina (Al_2O_3), widely used advanced ceramics, has applications in armor, aerospace, biomedicine, machinery, and chemicals due to its favorable properties, such as cost effectiveness, exceptional thermal resistance, chemical inertness, biocompatibility, high hardness, and wear resistance [1–6]. However, its inherent low fracture toughness hampers its overall mechanical performance and restricts its broader utility. Numerous endeavors have aimed to enhance the fracture toughness of Al_2O_3 ceramics, including techniques, such as refining grain size through specialized powder preparation methods and advanced sintering technologies [7–9], and incorporating diverse secondary phases, such as TiB_2, B_4C, SiC, ZrO_2, BN, and C with the forms of particles, whiskers, fibers, tubes, or plate-like materials [10–16]. Despite varying degrees of success attained by these toughening methods, the improvements are often marginal, accompanied by elevated production costs or challenges in large-scale manufacturing. Therefore, the continued exploration of novel methodologies for cost-effective, high-toughness Al_2O_3 ceramic production is imperative.

The integration of high-hardness ceramic particles, such as TiB_2, B_4C, and SiC, as secondary phases within the Al_2O_3 matrix, holds promise because these additives enhance fracture toughness while preserving the hardness, strength, and elastic modulus of the Al_2O_3 matrix. The commonly used preparation methods of these Al_2O_3 composite ceramics are directly mixing Al_2O_3 and secondary phase powders, and then hot pressing sintering or spark plasma sintering (SPS). For example, Parchoviansky *et al.* [17] prepared Al_2O_3–SiC composite ceramics by hot pressing at 1740 ℃ using Al_2O_3 and SiC powders as raw materials. The fracture toughness of the Al_2O_3–SiC composites containing different volume fractions of SiC is distributed in the range from 5.0 to 6.1 MPa·m$^{1/2}$. Deng *et al.* [18] prepared Al_2O_3–TiB_2 composite ceramics by mixing Al_2O_3 and TiB_2 powders, and subsequent hot pressing sintering at 1650–1800 ℃. The optimal fracture toughness, 5.2 MPa·m$^{1/2}$, is realized when the TiB_2 content is 30 vol%. Currently, despite the preparation of Al_2O_3 composite ceramics toughened by various ceramic particles, the toughening effects of these ceramic particles have yet to yield substantial breakthroughs; the achieved fracture toughness for Al_2O_3 composite ceramics range from

3.8 to 6.2 MPa·m$^{1/2}$ over years [10–19]. The primary reason for this limitation lies in the prevailing toughening structure shared by various Al_2O_3 composite ceramics toughened, wherein the secondary phases are independently dispersed within the Al_2O_3 matrix, as shown in Fig. 1(a). Despite variations in the types of secondary phases and sintering methods employed, the underlying toughening structure remains constant, leading to marginal differences in fracture toughness. The reported three-phase Al_2O_3 composite ceramics contain two types of secondary phases [20–23], but the different secondary phases are segregated from each other and independently dispersed within the Al_2O_3 matrix, as shown in Fig. 1(b). Consequently, the fundamental toughening structure in Figs. 1(a) and 1(b) remains analogous, limiting the enhancement of fracture toughness compared with two-phase Al_2O_3 composites. Therefore, the development of a novel toughening structure is essential to improve the fracture toughness of Al_2O_3 composite ceramics further.

In our previous studies [24,25], B_4C composite ceramics featuring TiB_2–SiC agglomerates as a secondary phase were synthesized, as shown in Fig. 1(c). Unlike conventional setups where TiB_2 and SiC remain isolated and individually dispersed, the secondary phase in these composites comprises interlocked TiB_2 and SiC entities. The existence of such TiB_2–SiC agglomerates remarkably elevates the toughness of B_4C–TiB_2–SiC composites from 4.6 to 6.5 MPa·m$^{1/2}$. The methodology used for preparation results in randomly formed TiB_2–SiC agglomerates within the B_4C matrix, rendering their size, structure, and content uncontrollable. However, these findings indicate that composite structural units as secondary phases can achieve better toughening effect compared with isolated, independently dispersed secondary phases because the multi-interface collaborative toughening behavior of the composite structural units can induce the multiple deflection of cracks, thus consuming a large amount of crack propagation energy.

Drawing inspiration from this work, adopting a toughening structure using composite structural units as secondary phases offers an effective approach to overcome the current toughening bottleneck faced by Al_2O_3 composite ceramics. The Al_2O_3 composite ceramics with composite structural units as secondary phase can be prepared by sintering using the mixture of Al_2O_3 powders and the powders possessing composite structure as raw materials. In this method, the controlled
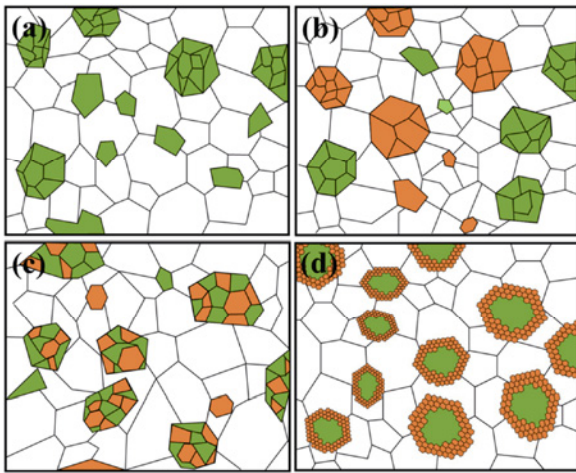
Fig. 1 Schematic diagram of microstructures of Al_2O_3 composite ceramics toughened by (a) single secondary phase, (b) two isolated and individually dispersed secondary phases, (c) agglomerates of two types of secondary phases, and (d) core–shell composite structural units.

advance preparation of the powders possessing the composite structure is key. Currently, the technology of preparing core–shell structural composite powders by the molten salt method has been widely reported with success [26,27]. In terms of the phase composition for the composite powders, B_4C and TiB_2 have ultrahigh hardness, relatively low density, and chemical inertness to Al_2O_3, and are ideal toughening phases for the Al_2O_3 matrix [28,29]. Therefore, core–shell structural powders consisting of B_4C and TiB_2 is a suitable candidate that can be mixed with Al_2O_3 powders to prepare the mixture for subsequent sintering.

In this work, the innovative notion of adopting core–shell composite structural units as secondary phases to enhance the toughness of the Al_2O_3 composite ceramics is introduced, as shown in Fig. 1(d). This breakthrough is achieved by crafting $B_4C@TiB_2$ core–shell units encapsulated within an Al_2O_3 matrix, employing a combined approach of molten salt

methodology and SPS. First, core–shell $B_4C@TiB_2$ powders are synthesized using B_4C and TiH_2 as precursors through the molten salt technique. Subsequently, the Al_2O_3 composite ceramics are fabricated by SPS using Al_2O_3 powders and synthesized $B_4C@TiB_2$ powders as starting materials. The microstructure and synthesis mechanism of the $B_4C@TiB_2$ powders are analyzed. The microstructure, compositions, and interfaces of the $B_4C@TiB_2$ core–shell units inside the Al_2O_3 matrix are studied. The mechanical properties and toughening mechanism of the Al_2O_3 composite ceramics toughened by $B_4C@TiB_2$ core–shell units are also discussed.

2 Materials and methods

2.1 Materials

Al_2O_3 powders with purity of $\geqslant$ 99.99% and average particle size of 0.2 um (Shanghai Aladdin Biochemical Technology Co., Ltd., China), B_4C powders with purity of $\geqslant$ 97% and average particle size of 5.0 μm (Jingangzuan Boron Carbide Co., Ltd., China), and TiH_2 powders with purity of $\geqslant$ 99% and particle size of $\leqslant$ 45 μm (Shanghai Aladdin Biochemical Technology Co., Ltd., China) were adopted as raw materials. NaCl and KCl powders with purity of $\geqslant$ 99% (Shanghai Aladdin Biochemical Technology Co., Ltd., China) were adopted as molten salt medium. The characteristics of these raw materials are shown in Fig. 2.

2.2 Preparation of core–shell structured $B_4C@TiB_2$ powders

A mixture of B_4C, TiH_2, NaCl, and KCl powders at mass ratios of 7 : 6 for B_4C and TiH_2, 1 : 1 for NaCl and KCl, and 1 : 4 for (B_4C+TiH_2) and (NaCl+KCl) was created. This blend was subjected to magnetic stirring in ethanol solution for 24 h, followed by drying
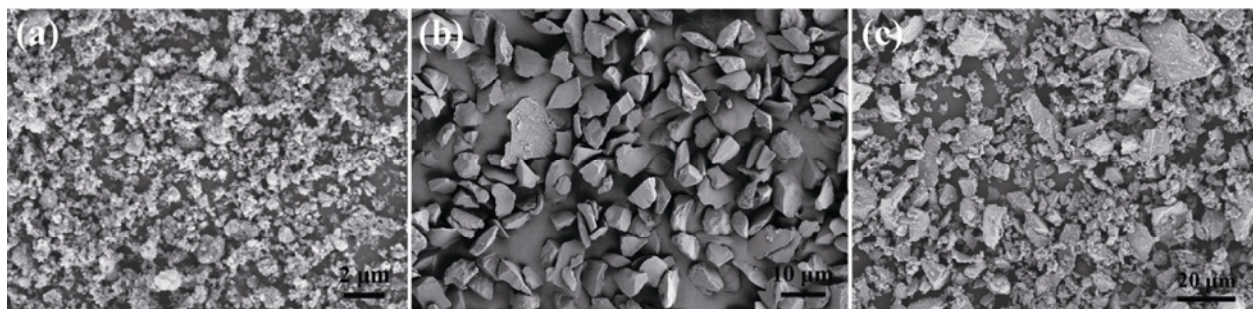
Fig. 2 SEM images of raw materials: (a) Al_2O_3 powders, (b) B_4C powders, and (c) TiH_2 powders.

using rotary evaporation and vacuum oven techniques, yielding a powdered mixture. This mixture was loaded into a corundum crucible equipped with a cap and subjected to calcination within a tube furnace under a flowing argon atmosphere. The process involved heating at a rate of 2 ℃/min to a calcination temperature of 1400 ℃ and dwelling time of 2 h. Following cooling to the ambient temperature, the calcined mixture underwent a triple washing sequence using water, hydrochloric acid, and water, and is subsequently dried in a vacuum oven for 24 h, resulting in the prepared $B_4C@TiB_2$ powders.

2. 3   Preparation of Al_2O_3–$B_4C@TiB_2$ composite ceramics

The Al_2O_3 composite ceramics containing 10 wt% $B_4C@TiB_2$ core–shell units were designed. First, Al_2O_3 and synthesized $B_4C@TiB_2$ powders, at a mass ratio of 9 : 1, were mixed in ethanol via magnetic stirring for 24 h. After drying and passing through a 200-mesh sieve, a powder mixture of Al_2O_3 and $B_4C@TiB_2$ was obtained. This mixture was loaded into a cylindrical graphite die with an inner diameter of 30 mm. The interior surfaces of the die and the punches were covered with a thin graphite foil, and the exterior of the die was encased in an 8 mm thick graphite felt. Sintering was conducted within a spark plasma sintering furnace (HPD 60/0, FCT Systeme GmbH, Germany). The samples were rapidly heated to 600 ℃ within 2 min and then 100 ℃/min up to 1600 ℃, dwelling for 5 min. An uniaxial pressure of 30 MPa was applied at 600 ℃, maintained through 800 ℃, and sustained throughout sintering. Then, the samples were cooled, and the pressure was released by turning off the power.

2. 4   Characterizations

The phase components of powders and ceramics were characterized using an X-ray diffractometer (XRD; X'Pert PRO, PANalytical, the Netherlands) with Cu Kα radiation (40 kV, 40 mA). The microstructures of powders and ceramics were observed using a scanning electron microscope (SEM; S4800, Hitachi, Japan) coupled with an energy-dispersive X-ray analyzer system (EDS). Ceramic composite density was determined using Archimedes method, and the relative density is calculated by dividing the actual density by the theoretical density. Vickers hardness was evaluated with 10 × 9.8 N load applied for 15 s to the polished surface. Fracture toughness was calculated from the

length of the cracks of Vickers indentations according to Eq. (1) [30].

$$K_{IC} = \chi \left(\frac{E}{H_V} \right)^{1/2} \frac{P}{c^{3/2}} \tag{1}$$

where E is the Young's modulus, H_V is the Vickers hardness, c is the average of all radial crack length measured from the center of the indent, P is the applied load, and χ is an empirical calibration constant, which is 0.016±0.004. The reported density, fracture toughness, and Vickers hardness values represent averages from 5, 7, and 3 measurements, respectively.

3   Results and discussion

A schematic of the formation processes for the Al_2O_3 composite ceramics toughened by $B_4C@TiB_2$ core–shell units is shown in Fig. 3. The initial step involves uniform mixing of B_4C, TiH_2, $NaCl$, and KCl powders, which undergo heating. As the temperature increases, TiH_2 breaks down into nanosized Ti powders and H_2 at approximately 430 ℃ [31], and subsequently, NaCl and KCl powders liquefy at approximately 658 ℃ [32]. The nanosized Ti and micron-sized B_4C particles are rearranged, uniformly dispersing within the liquid medium. Upon reaching the reaction temperature of B_4C and Ti, the nanosized Ti particles commence reacting on the surface of micron-sized B_4C particles, engendering the formation of a TiB_2 shell along with a minor quantity of C based on Reaction (2). With extended reaction duration, the thickness of the TiB_2 shell progressively increases until the total consumption of Ti. The surplus B_4C in the core of B_4C particles remains unreacted due to the excess B_4C powder in the raw materials, culminating in the formation of the core–shell structured $B_4C@TiB_2$ powders. Subsequently, the synthesized $B_4C@TiB_2$ powders are mixed with the Al_2O_3 powders, generating the initial sintering powders. Finally, SPS is performed to fabricate the targeted Al_2O_3–$B_4C@TiB_2$ composite ceramics.

$$(1 + x)B_4C + 2Ti = xB_4C + 2TiB_2 + C \ (x > 0) \tag{2}$$
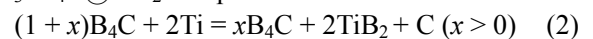
3. 1 $B_4C@TiB_2$ powder characteristics

The progressive development of the $B_4C@TiB_2$ powders is depicted in Fig. 3. Micron-sized B_4C powders are deliberately employed in excess to ensure B_4C within the core of the B_4C particles remains intact, and a controlled scarcity of TiH_2, which can decompose
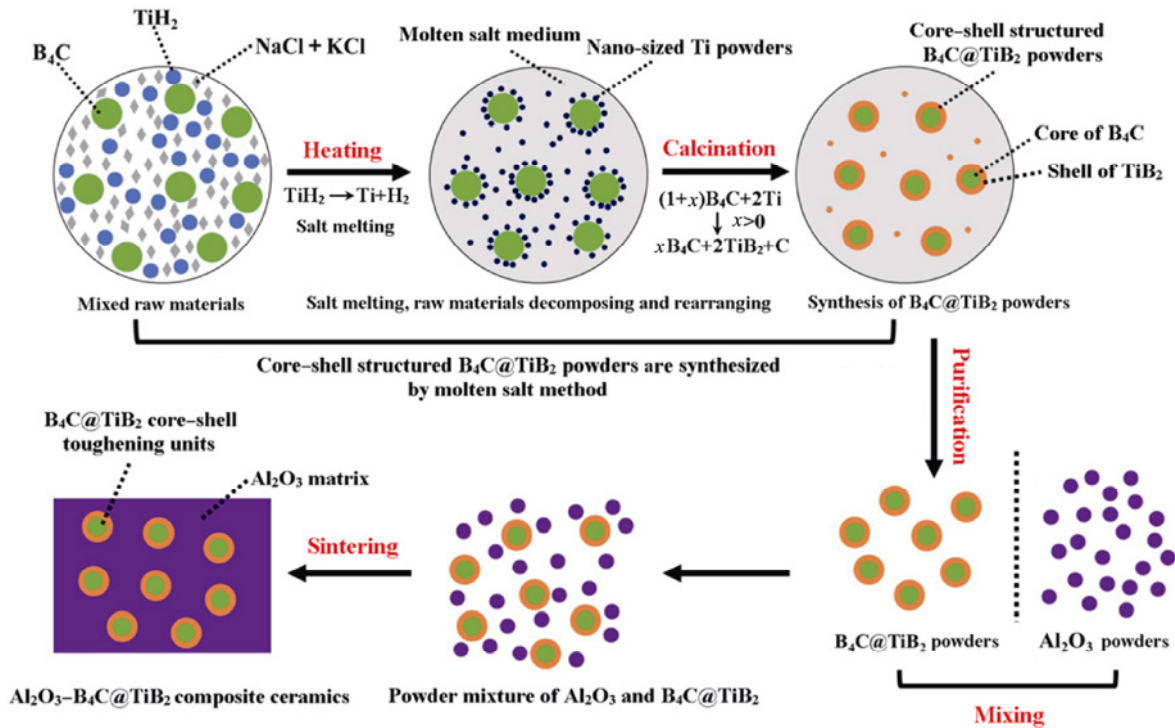
Fig. 3 Schematic illustration for formation processes of Al_2O_3 composite ceramics toughened by $B_4C@TiB_2$ core–shell units.

into nanosized Ti powders, is adopted to ensure nanosized Ti particles react on the surface of the micron-sized B_4C particles, ultimately forming the TiB_2 shell. The thickness of the TiB_2 shell can be fine-tuned by adjusting the ratio of B_4C to TiH_2.

Figure 4(a) shows the XRD pattern of the $B_4C@TiB_2$ powders. Only peaks corresponding to B_4C and TiB_2 are detected, indicating the composite powders' B_4C and TiB_2 composition. The absence of a peak for C is attributed to its negligible quantity and low atomic weight [26]. The microstructure of the $B_4C@TiB_2$ powders, as indicated in Fig. 4(b), illustrates the surface of $B_4C@TiB_2$ particles becomes textured. However, their shape and size distribution remain largely unchanged compared with the original B_4C particle powders. Importantly, fractured particles revealing a partial shell detachment, as highlighted in the rectangular area of Fig. 4(b), reaffirm the presence of a distinct core–shell configuration. EDS analysis in Figs. 4(c) and 4(d) indicates point 1, selected on the core, primarily comprises B and C, and point 2, chosen from the shell, mainly consists of Ti and B. This analysis, coupled with the XRD outcomes, confirms the core as B_4C and the shell as TiB_2. The rectangular region of Fig. 4(b) is magnified in Fig. 4(e) to gain deeper insight into $B_4C@TiB_2$ particle's microstructure. The

core's surface displays rugged features, marked by gullies, distinctly differing from the smooth surface of raw B_4C powders. This alteration substantiates the *in situ* reaction between B_4C and Ti on the particle's surface. The shell encompasses numerous nanosized TiB_2 grains spanning 10–100 nm, with an approximate thickness of 500 nm. The EDS element mapping images in Figs. 4(f)–4(h) for this region further validate the core as B_4C and the shell as TiB_2. These analyses affirm the successful synthesis of core–shell structured $B_4C@TiB_2$ powders, with the core composed of micron-sized B_4C particles and the shell comprising numerous nanoscale TiB_2 particles.

3. 2 Microstructure and mechanical properties of Al_2O_3–$B_4C@TiB_2$ composite ceramics

The phase constituents of the Al_2O_3–$B_4C@TiB_2$ composite ceramics are characterized through XRD patterns, as shown in Fig. 5(a). The XRD analysis demonstrates the presence of Al_2O_3, B_4C, and TiB_2, affirming the retention of $B_4C@TiB_2$ powder components within the Al_2O_3 matrix after sintering. No new phases emerge, indicating the preservation of initial components during sintering. The backscattered electron (BSE) image of the polished surface of the composite ceramics in Fig. 5(b) delineates three distinct phase
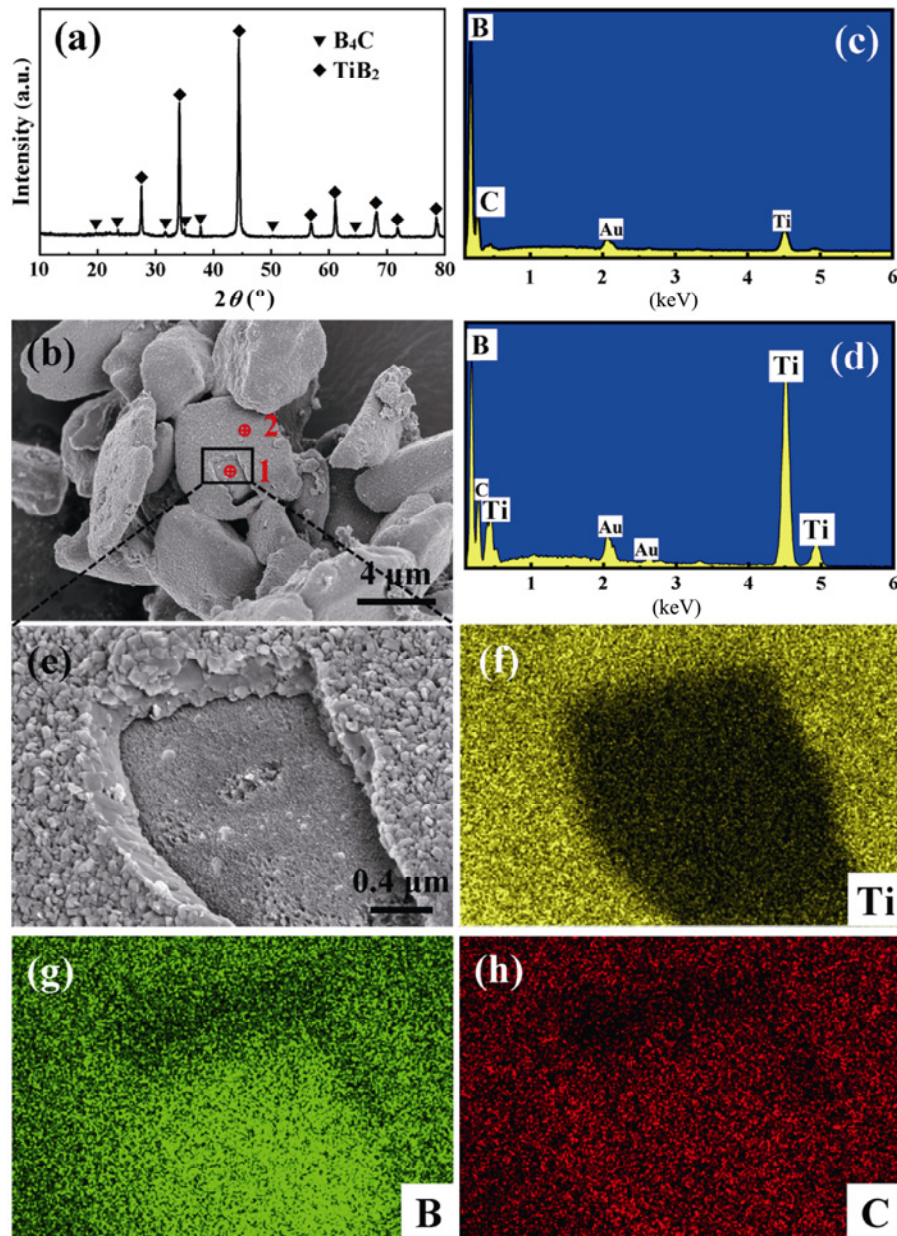
Fig. 4 (a) XRD pattern and (b) SEM image of $B_4C@TiB_2$ powders. (c, d) EDS analysis for points 1 and 2 in (b), respectively. (e) Magnification for rectangular in (b). (f–h) EDS element mapping images for (e).
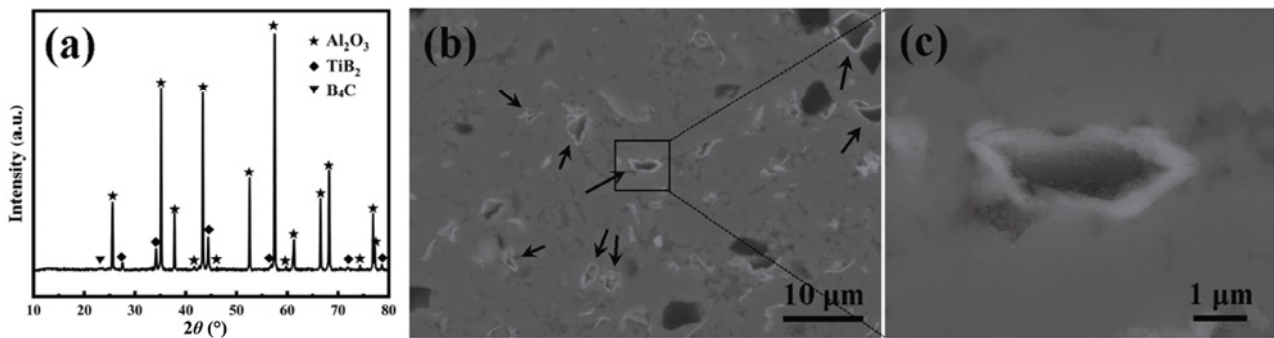

Fig. 5 (a) XRD pattern and (b) BSE image of polished surface of Al_2O_3–$B_4C@TiB_2$ composite ceramics. (c) Magnification for rectangular in (b).

components. The glossy white regions correspond to TiB$_2$, the dark gray regions indicate B$_4$C, and the remaining gray regions denote Al$_2$O$_3$. The surface hardly exhibits pores, demonstrating the ceramics' high density. Intact B$_4$C@TiB$_2$ core–shell units are discernible (indicated by arrows). An amplified view of a typical B$_4$C@TiB$_2$ core–shell unit in Fig. 5(c) offers further insight into the composite structure units. Within this unit, the B$_4$C is completely encapsulated by the TiB$_2$, and the TiB$_2$ shell is approximately 500 nm in thickness, consistent with the shell thickness in the B$_4$C@TiB$_2$ powders in Fig. 4(e). Interfaces between B$_4$C–TiB$_2$ and TiB$_2$–Al$_2$O$_3$ exhibit strong interfacial compatibility. The analysis indicates the preservation of the B$_4$C@TiB$_2$ core–shell structure within the Al$_2$O$_3$ matrix after sintering, thereby accomplishing the targeted Al$_2$O$_3$ composite ceramics toughened by B$_4$C@TiB$_2$ core–shell units. Independently dispersed TiB$_2$ and B$_4$C phases also exist within the Al$_2$O$_3$ matrix due to the disruption of the core–shell structure of B$_4$C@TiB$_2$ powders prior to sintering. Mechanical impacts during the powder handling of removal from the corundum crucible, water washing, sieving, and mechanical mixing with Al$_2$O$_3$ powders may have damaged the core–shell structure. This outcome is corroborated by Figs. 4(b) and 4(e), verifying the structure's disruption. TiB$_2$ detaches from B$_4$C@TiB$_2$ powders, and the remaining B$_4$C disperses within the

starting sintering powders. This result leads to the formation of independently dispersed TiB$_2$ and B$_4$C within the Al$_2$O$_3$ matrix after sintering. Although the diffusion of TiB$_2$ during sintering can also contribute to this phenomenon, the sintering temperature of 1600 ℃ is relatively low for B$_4$C and TiB$_2$, whose typical sintering temperature range is 1900–2200 ℃ [33,34]. The fast heating rate and short sintering time adopted in this paper minimize diffusion effects [35–38]. Therefore, the diffusion is not the main reason for core–shell structure disruption.

Figure 6(a) presents the SEM image of the composite ceramics' fracture surface. The fracture surface displays a rugged topography characterized by undulations and depressions. Numerous micron-sized bulged grains and sunken cavities are encompassed by a covering layer, as marked by arrows. A representative region is magnified, as shown in Fig. 6(b), which shows a bulging micron-sized grain (marked by point 1) enclosed by a shell approximately 500 nm in thickness, composed of numerous nanosized grains (marked by point 2). A shell without a core is also observed (marked by point 3), which is the relic that the core is pulled out. EDS analysis conducted at point 1 confirms the micron-sized grain is B$_4$C, and the results from points 2 and 3 verify the shell is TiB$_2$. The above observations show the typical core–shell structure of the toughening units and their fracture paths during the
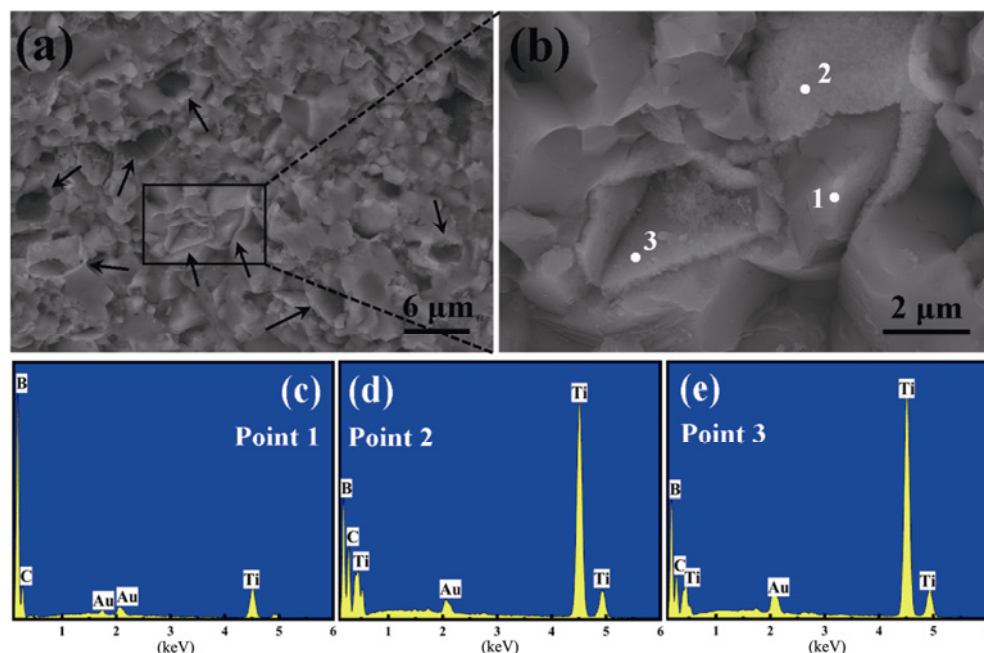
Fig. 6 (a) SEM image of fracture surface of Al$_2$O$_3$–B$_4$C@TiB$_2$ composite ceramics. (b) Magnification for rectangular in (a). (c–e) EDS analysis for points 1, 2, and 3 in (b), respectively.

fracture of the composite ceramics. In the core–shell toughening units, the core consists of micron-sized B_4C grains, and the shell comprises numerous nanosized TiB_2 grains, a composition identical to the microstructure of the $B_4C@TiB_2$ powders. The size of the TiB_2 grains in the toughening units experiences minimal growth compared with those in the $B_4C@TiB_2$ powders because the grain growth temperature for TiB_2 is approximately 1700 ℃ [39], higher than the sintering temperature of 1600 ℃. Multidimensional fracture modes are evident within this localized region. Intergranular fracture emerges along the interface of the micron-sized Al_2O_3 grain and the outer side of the TiB_2 shell layer, and the micron-sized B_4C grain and the inner side of the TiB_2 shell layer. In addition, the TiB_2 shell layer itself fractures, forming a generated cross section that bridges the interfaces on both sides of the shell layer. Furthermore, within the interior of the shell layer, intergranular fracture occurs amidst the nanosized TiB_2 grains, consistent with the fracture mode observed in TiB_2 ceramics [40]. This amalgamation of multidimensional fracture modes contributes to the enhancement of composite ceramics' fracture toughness.

The relative density, Vickers hardness, and fracture toughness of the Al_2O_3–$B_4C@TiB_2$ composite ceramics, along with other referenced Al_2O_3 composite ceramics [10,11,16,17,21], are listed in Table 1. The relative density of the Al_2O_3–$B_4C@TiB_2$ composite ceramics is 99.7%±0.2%, indicating approximately complete density. The result agrees with the SEM image in Fig. 5(b). The high relative density is pivotal to ensuring excellent mechanical properties. The Vickers hardness of the ceramics achieved in this paper is 21.5±0.8 GPa, surpassing that of other Al_2O_3 composite ceramics. This heightened hardness in the Al_2O_3–$B_4C@TiB_2$ composite ceramics arises from two key factors: the high relative density of the composite ceramics itself, which is the basic guarantee for high

hardness, and the ultrahigh inherent hardness of B_4C and TiB_2 (29–41 GPa [36,41,42] and 25–35 GPa [39,40,43], respectively), which can elevate the hardness of the Al_2O_3 matrix. Notably, the fracture toughness of the Al_2O_3–$B_4C@TiB_2$ composite ceramics reaches an impressive 6.92±0.22 MPa·m$^{1/2}$, outperforming other Al_2O_3 composite ceramics. This advancement can be attributed to the formation of $B_4C@TiB_2$ core–shell toughening units, which induce a multidimensional fracture mode within the composite ceramics. This mode effectively absorbs substantial crack propagation energy compared with the approach of independently dispersed toughening phases.

3.3 Toughening mechanism of Al_2O_3–$B_4C@TiB_2$ composite ceramics

Within the vicinity of the core–shell toughening units, micron-sized Al_2O_3 matrix grains, micron-sized B_4C grains, and nanosized TiB_2 grains coexist. Simultaneously, the micron-sized B_4C core is completely enclosed by a shell layer consisting of nanosized TiB_2 grains. The thermal expansion coefficients of Al_2O_3 ($7.2×10^{-6}$ K^{-1} [44]), B_4C ($4.5×10^{-6}$ K^{-1} [24]), and TiB_2 ($8.1×10^{-6}$ K^{-1} [24,45]) differ remarkably. This localized region features a distinctive geometric configuration that amalgamates multidimensional variations in phase types, grain size, and thermal expansion coefficients. Consequently, an intricate stress distribution is established around the core–shell units. This complexity underscores the potential influence of $B_4C@TiB_2$ core–shell units on the toughening mechanism when introduced as a composite toughening phase within the Al_2O_3 composite ceramics. This mechanism may deviate from the approach observed in Al_2O_3 composite ceramics, which are toughened by isolated, independently distributed secondary phases.

The propagation of cracks within the Al_2O_3–$B_4C@TiB_2$ composite ceramics is presented in Figs. 7(a) and 7(b), highlighting the BSE images of polished

Table 1　Relative density and mechanical properties of Al_2O_3 composite ceramics

Sample	Relative density (%)	Vickers hardness (GPa)	Fracture toughness (MPa·m$^{1/2}$)	Preparation method	Ref.
Al_2O_3–$B_4C@TiB_2$	99.7±0.2	21.5±0.8	6.92±0.22 (IND)	SPS	This work
Al_2O_3–TiC	—	17.1–19.4	4.98–6.14 (IND)	Hot pressing	[10]
Al_2O_3–TiB_2	—	18.5–24.1	4.27–5.40 (CN)	SPS	[11]
Al_2O_3–Ti_3SiC_2	96.0–98.0	18.6–22.6	5.1–6.2 (IND)	Hot pressing	[16]
Al_2O_3–SiC	98.7–99.5	18.4–20.3	5.0–6.1 (IND)	Hot pressing	[17]
Al_2O_3–TiB_2	98.5–99.9	19.6–21.3	3.7–5.2 (IND)	Hot pressing	[18]
Al_2O_3–TiB_2–$TiSi_2$	—	~16.9	~4.7 (IND)	Hot pressing	[21]

Note: IND refers to indentation method; CN refers to Chevron notch.
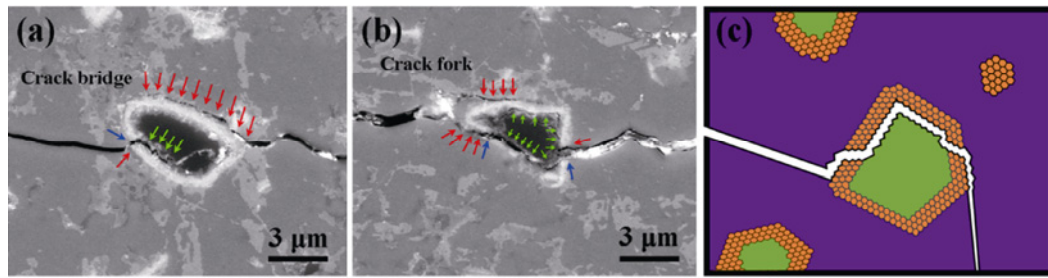
Fig. 7　(a, b) BSE images of polished surface with cracks of Al_2O_3–$B_4C@TiB_2$ composite ceramics. (c) Schematic diagram for crack propagation in regions surrounding core–shell units.

surfaces bearing cracks. The modes of crack propagation can be analyzed from two perspectives. First, the $B_4C@TiB_2$ core–shell unit is regarded as a unified entity. When cracks traverse these units, they generate crack bridges and forks around them, which is similar to the crack propagation pattern observed in Al_2O_3 ceramics toughened by independently distributed B_4C or TiB_2 phases [4,11]. However, further analysis of crack propagation within the interior of these core–shell units is warranted upon considering the $B_4C@TiB_2$ core–shell units as composite structures. As the crack propagates to the external interface of the core–shell units, the direction of propagation deflects along the interface between the Al_2O_3 matrix and TiB_2 shell layer, as indicated by the red arrows. Subsequently, the crack deflects into the shell layer consisting of nanosized TiB_2 grains and traverses this layer by propagating along the interface of these nanosized TiB_2 grains, allowing it to enter the interior of the core–shell units, as indicated by the blue arrows. The subsequent change in crack propagation direction occurs along the interface between the shell layer of TiB_2 and the core of the B_4C grain, as indicated by the green arrows. Subsequently, the cracks traverse once more through the shell layer consisting of nanosized TiB_2 grains and then continue to propagate along the interface between the shell layer of TiB_2 and the Al_2O_3 matrix. Finally, the cracks exit the core–shell units and enter the Al_2O_3 matrix. During the above process, the crack may halt at any location where the energy require for crack propagation is completely consumed. The schematic portraying the deflection of cracks in the region around core–shell units is presented in Fig. 7(c). Therefore, the existence of $B_4C@TiB_2$ core–shell units within the Al_2O_3 matrix generates a complex stress distribution that induces cracks to deflect in multiple dimensions, remarkably consuming crack propagation energy. This behavior leads to an enhancement in the fracture toughness of Al_2O_3 ceramics.

4　Conclusions

In this paper, an Al_2O_3 composite ceramics toughened by $B_4C@TiB_2$ core–shell units are successfully fabricated through a combination of the molten salt method and SPS. The synthesis of $B_4C@TiB_2$ core–shell toughening units stems from the prior production of core–shell structural $B_4C@TiB_2$ powders, and this core–shell structure is effectively preserved within the Al_2O_3 matrix after sintering. The $B_4C@TiB_2$ core–shell unit consists of a micron-sized B_4C core enclosed by a shell approximately 500 nm in thickness, composed of numerous nanosized TiB_2 grains. The area encompassing the core–shell unit exhibits a distinct geometric arrangement amalgamating multidimensional differences in phase types, grain sizes, and thermal expansion coefficients. Consequently, an intricate stress distribution ensues. When viewing the $B_4C@TiB_2$ core–shell unit as an entirety, crack bridges and crack forks are generated around the units. Alternatively, the crack path sequentially traverses along the interface of the Al_2O_3 matrix and TiB_2 shell layer when interpreting the $B_4C@TiB_2$ core–shell units as composite structures. Then, it proceeds through the internal interface of the nanosized TiB_2 shell layer, followed by propagation along the interface of the TiB_2 shell layer and the B_4C core, and subsequently along the internal interface of the nanosized TiB_2 shell layer. Ultimately, the crack proceeds along the interface of the TiB_2 shell layer and the Al_2O_3 matrix. The crack along the internal interface of the nanosized TiB_2 shell layer bridges the cracks on either side of the shell layer. Therefore, the existence of core–shell units induces the multidimensional deflection of cracks, necessitating a considerable amount of crack propagation energy. This phenomenon ultimately enhances the fracture toughness of the Al_2O_3 matrix. The resulting Al_2O_3–$B_4C@TiB_2$ displays relative density of 99.7%±0.2%, Vickers hardness of 21.5±0.8 GPa, and fracture toughness 6.92±0.22 MPa·m$^{1/2}$.

This novel concept, the preparation methodology, and the elucidated toughening mechanism of utilizing core–shell units as a secondary phase to enhance ceramic matrix toughness offer a new perspective and theoretical foundation for the toughening of other structural ceramics.

Acknowledgements

Declaration of competing interest

The authors have no competing interests to declare that are relevant to the content of this article.

References

[1] Huang ZH, Pan W, Qi LH, *et al*. Study on the erosive wear behavior of Al_2O_3 ceramics. *Rare Metal Mat Eng* 2003, **32**: 277–280.

[2] Qiu LK, Li XK, Peng Y, *et al*. Types, performance and application of AI_2O_3 system ceramic cutting tool. *J Rare Earths* 2007, **25**: 322–326.

[3] Lu SZ, Yang QH. Fluorescence characteristics of Al_2O_3 transparent ceramics. *Chin J Inorg Chem* 2009, **25**: 1642–1645. (in Chinese)

[4] Guo WM, Zhang ZL, Li JX, *et al*. Improvement of densification and mechanical properties of Al_2O_3–B_4C ceramics. *Ceram Int* 2016, **42**: 11486–11489.

[5] Prashar G, Vasudev H. High temperature erosion behavior of plasma sprayed Al_2O_3 coating on AISI-304 stainless steel. *World J Eng* 2021, **18**: 760–766.

[6] Zeng Y, Zhang ZJ, Sun LJ, *et al*. Atmosphere debinding heat treatment of 3D printed alumina ceramics. *J Inorg Mater* 2022, **37**: 333.

[7] Yuan Y, Fan JY, Li JS, *et al*. Oscillatory pressure sintering of Al_2O_3 ceramics. *Ceram Int* 2020, **46**: 15670–15673.

[8] Wang XT, Padture NP, Tanaka H, *et al*. Wear-resistant ultra-fine-grained ceramics. *Acta Mater* 2005, **53**: 271–277.

[9] Liu JL, Wang YG, Yang FQ, *et al*. Grain refining in spark plasma sintering Al_2O_3 ceramics. *J Alloys Compd* 2015, **622**: 596–600.

[10] Li ZL, Zhao J, Sun JL, *et al*. Reinforcement of Al_2O_3/TiC ceramic tool material by multi-layer graphene. *Ceram Int* 2017, **43**: 11421–11427.

[11] Rubino F, Rotella G, Perrella M, *et al*. Microstructural and mechanical properties of Al_2O_3 and Al_2O_3/TiB_2 ceramics consolidated by plasma pressure compaction. *J Mater Eng Perform* 2023, **32**: 4391–4403.

[12] Du WY, Ai YL, He W, *et al*. Formation and control of "intragranular" ZrO_2 strengthened and toughened Al_2O_3 ceramics. *Ceram Int* 2020, **46**: 8452–8461.

[13] Lv HX, Zhou Q, Su YF, *et al*. High damage tolerant Al_2O_3 composite ceramics constructed with short Al_2O_3 fibers. *Int J Appl Ceram Tec* 2023, **20**: 2700–2707.

[14] Swarnakar AK, Huang SG, Van der Biest O, *et al*. Ultrafine Al_2O_3–B_4C composites consolidated by pulsed electric current sintering. *J Alloys Compd* 2010, **499**: 200–205.

[15] Zhang SC, Fahrenholtz WG, Hilmas GE, *et al*. Pressureless sintering of carbon nanotube–Al_2O_3 composites. *J Eur Ceram Soc* 2010, **30**: 1373–1380.

[16] Chin YL, Tuan WH. Contribution of plastic deformation of Ti_3SiC_2 to the crack deflection in the Al_2O_3/Ti_3SiC_2 composites. *Mat Sci Eng A-Struct* 2011, **528**: 3270–3274.

[17] Parchoviansky M, Galusek D, Sedláček J, *et al*. Microstructure and mechanical properties of hot pressed Al_2O_3/SiC nanocomposites. *J Eur Ceram Soc* 2013, **33**: 2291–2298.

[18] Deng JX, Cao TK, Liu LL. Self-lubricating behaviors of Al_2O_3/TiB_2 ceramic tools in dry high-speed machining of hardened steel. *J Eur Ceram Soc* 2005, **25**: 1073–1079.

[19] Krishnan SV, Ambalam MM, Venkatesan R, *et al*. Technical review: Improvement of mechanical properties and suitability towards armor applications—Alumina composites. *Ceram Int* 2021, **47**: 23693–23701.

[20] Shi SF, Sekino T, Cho S, *et al*. Ti and TiC co-toughened Al_2O_3 composites by *in situ* synthesis from reaction of Ti and MWCNT. *Mat Sci Eng A-Struct* 2020, **777**: 139066.

[21] Li MS, Huang CZ, Zhao B, *et al*. Mechanical properties and microstructure of Al_2O_3–TiB_2–$TiSi_2$ ceramic tool material. *Ceram Int* 2017, **43**: 14192–14199.

[22] Zhao DK, Wu DJ, Shi J, *et al*. Microstructure and mechanical properties of melt-grown alumina-mullite/glass composites fabricated by directed laser deposition. *J Adv Ceram* 2022, **11**: 75–93.

[23] Sun LC, Zhou C, Du TF, *et al*. Directionally solidified Al_2O_3/$Er_3Al_5O_{12}$ and Al_2O_3/$Yb_3Al_5O_{12}$ eutectic ceramics prepared by optical floating zone melting. *J Inorg Mater* 2021, **36**: 652–658.

[24] Zhang XR, Zhang ZX, Liu YM, *et al*. High-performance B_4C–TiB_2–SiC composites with tuneable properties fabricated by reactive hot pressing. *J Eur Ceram Soc* 2019, **39**: 2995–3002.

[25] Zhang XR, Zhang ZX, Wang WM, *et al*. Microstructure and mechanical properties of B_4C–TiB_2–SiC composites toughened by composite structural toughening phases. *J Am Ceram Soc* 2017, **100**: 3099–3107

[26] Ren DL, Deng QH, Wang J, *et al*. Synthesis and properties

of conductive B$_4$C ceramic composites with TiB$_2$ grain network. *J Am Ceram Soc* 2018, **101**: 3780–3786.

[27] Shao JQ, Li M, Chang KK, *et al*. Fabrication and characterization of SPS sintered SiC-based ceramic from Y$_3$Si$_2$C$_2$-coated SiC powders. *J Eur Ceram Soc* 2018, **38**: 4833–4841.

[28] Guo WM, Zhang ZL, Li JX, *et al*. Improvement of densification and mechanical properties of Al$_2$O$_3$–B$_4$C ceramics. *Ceram Int* 2016, **42**: 11486–11489.

[29] Chen BS, Xiao GC, Yi MD, *et al*. Mechanical properties and microstructure of Al$_2$O$_3$/TiB$_2$ and Al$_2$O$_3$/TiB$_2$/GNPs ceramic tool materials prepared by spark plasma sintering. *Ceram Int* 2021, **47**: 11748–11755.

[30] Anstis GR, Chantikul P, Lawn BR, *et al*. A critical evaluation of indentation techniques for measuring fracture toughness: I, direct crack measurements. *J Am Ceram Soc* 1981, **64**: 533–538.

[31] Zhou YL, Zheng LR, Chu SQ, *et al*. *In-situ* EXAFS study on the thermal decomposition of TiH$_2$. *Chin Phys C* 2014, **38**: 038001.

[32] Liu XF, Fechler N, Antonietti M. Salt melt synthesis of ceramics, semiconductors and carbon nanostructures. *Chem Soc Rev* 2013, **42**: 8237–8265.

[33] Moshtaghioun BM, Cumbrera-Hernández FL, Gómez-García D, *et al*. Effect of spark plasma sintering parameters on microstructure and room-temperature hardness and toughness of fine-grained boron carbide (B$_4$C). *J Eur Ceram Soc* 2013, **33**: 361–369.

[34] Demirskyi D, Agrawal D, Ragulya A. Tough ceramics by microwave sintering of nanocrystalline titanium diboride ceramics. *Ceram Int* 2014, **40**: 1303–1310.

[35] Wang C, Wang X, Zhao Z. Microstructure homogeneity control in spark plasma sintering of Al$_2$O$_3$ ceramics. *J Eur Ceram Soc* 2011, **31**: 231–235.

[36] Zhang XR, Zhang ZX, Wen RL, *et al*. Comparisons of the densification, microstructure and mechanical properties of boron carbide sintered by hot pressing and spark plasma sintering. *Ceram Int* 2018, **44**: 2615–2619.

[37] Liu JG, Li Y, Cheng CG, *et al*. Study on the toughening mechanism of *in situ* synthesis (Ti$_x$Zr$_{1-x}$)B$_2$ in solid-state sintered SiC composite ceramics. *J Eur Ceram Soc* 2023, **43**: 760–767.

[38] Liu JG, Li Y, Li Y, *et al*. Microstructure and mechanical properties of SiC composite ceramics modified by

(Ti$_x$Zr$_{1-x}$)B$_2$ solid solution. *Ceram Int* 2023, **49**: 32261–32270.

[39] Zhang ZH, Shen XB, Wang FC, *et al*. Densification behavior and mechanical properties of the spark plasma sintered monolithic TiB$_2$ ceramics. *Mat Sci Eng A-Struct* 2010, **527**: 5947–5951.

[40] Wu N, Xue FD, Yang HL, *et al*. Effects of TiB$_2$ particle size on the microstructure and mechanical properties of TiB$_2$-based composites. *Ceram Int* 2019, **45**: 1370–1378.

[41] Zhang XR, Zhang ZX, Nie B, *et al*. Microstructure and mechanical properties of fine-grained boron carbide ceramics fabricated by high-pressure hot pressing combined with high-energy ball milling. *Ceram Int* 2018, **44**: 10766–10772.

[42] Zhao J, Wang D, Jin X, *et al*. Highly electro-conductive B$_4$C–TiB$_2$ composites with three-dimensional interconnected intergranular TiB$_2$ network. *J Adv Ceram* 2023, **12**: 182–195.

[43] Golla BR, Mukhopadhyay A, Basu B, *et al*. Review on ultra-high temperature boride ceramics. *Prog Mater Sci* 2020, **111**: 100651.

[44] Ryu SH, Park JH, Lee CS, *et al*. Experimental measurement of coefficient of thermal expansion for graded layers in Ni–Al$_2$O$_3$ FGM joints for accurate residual stress analysis. *Mater Trans* 2009, **50**: 1553–1557.

[45] Zhang XR, Zhang ZX, Wang WM, *et al*. Preparation of B$_4$C composites toughened by TiB$_2$–SiC agglomerates. *J Eur Ceram Soc* 2017, **37**: 865–869.